Bulletin of the Seismological Society of America, Vol. 95, No. 5, pp. 1731–1748, October 2005, doi: 10.1785/0120040105

Attenuation, Seismic Moments, and Site Effects for Weak-Motion Events: Application to the Pyrenees

by Stéphane Drouet, Annie Souriau, and Fabrice Cotton

Abstract We derive attenuation models, site response functions, and source parameters from small-magnitude events recorded at a regional scale. Our data set consists of 45 Pyrenean events with magnitude 2.7 to 5.4, recorded at distances from 15 to 200 km, for which about 600 displacement spectra could be computed.

We assume that the far-field displacement spectrum is the product of source, propagation, and site effects. *S*-wave displacement spectra are computed for accelerometric and velocimetric records using fast Fourier transforms by integration in the frequency domain for 0.5–15 Hz. Owing to the velocimeter response, the spectra may be unreliable below 1 Hz. A Brune-type source is assumed. Attenuation is decomposed into a frequency-dependent term (anelastic attenuation) and a non-frequency-dependent term (geometric attenuation). Adapting a process proposed by Scherbaum and Wyss (1990), we invert the data with a two-step regression. The first step recovers the geometric attenuation, the seismic moment, and a frequency-independent scaling factor. The second step gives the corner frequency, the anelastic attenuation, and a frequency-dependent site effect.

Our results show that the propagation term includes a slightly superspheric geometric attenuation that varies as $1/r^{1.2}$ and an anelastic attenuation that cannot be safely resolved with a linear approach. Computed moment magnitudes are generally 0.5 to 1 unit smaller than local magnitudes. Corner frequencies decrease linearly with magnitude, and the stress drops obtained appear to be nearly constant whatever the magnitude. Finally, robust site responses are computed that are compatible with those derived with other methods.

Introduction

Strong-motion prediction is a big challenge. In Europe, empirical strong ground motion models (e.g. Ambraseys *et al.*, 1996; Sabetta and Pugliese, 1996; Berge-Thierry *et al.*, 2003) have been built from very heterogeneous databases, which include records collected for various tectonic contexts. Moreover, these strong-motion databases are still dominated by analog instrument records, and the associated parameters (magnitude, earthquake location) have been derived using different procedures. Hardly any region in Europe can therefore be associated with a specific regional strong ground motion model, most regions having none at all. This lack of regional models is at present a weakness in the chain of seismic risk evaluation. It is caused by the fact that there are not enough strong-motion records to derive regional-specific empirical models.

However, in most European regions, large databases on small earthquakes are available. Associated parameters (magnitude, earthquake location) have been determined homogeneously. The use of such weak-motion data to derive strong-motion predictive relationships is thus a key goal of earthquake engineering (e.g., Boore, 1983; Andrews, 1986; Boatwright *et al.*, 1991; Malagnini *et al.*, 1999; Raoof *et al.*, 1999; Bay *et al.*, 2003). In order to use these weak motions to predict strong motions, it is essential to specify the physical mechanisms that control earthquake ground motion. These mechanisms are not yet completely understood and many questions are still being discussed:

1. The geometric decay found in some weak-motion studies appears to be superspheric (e.g., Frankel *et al.*, 1990, dependence up to r^{-2}). On the other hand, in some empirical strong ground motion studies, a geometric decay in r^{-1} leads to a negative Q (e.g., Ambraseys *et al.*, 1996; Boore *et al.*, 1997; Berge-Thierry *et al.*, 2003). The superspheric amplitude decay has been ascribed to the reflection of the upgoing direct wave at the base of the layer above the focus (Frankel, 1991), and to scattering (Gagnepain-Beyneix, 1987). According to these phenomena, the geometrical decay should therefore be strongly dependent on the depth of the focus. On the other hand,

since large earthquakes are not point sources, but extended finite sources that generate seismic waves at different depths, the scaling of the geometrical spreading might not be the same for small and large earthquakes. Finally, reliable attenuation models are also needed to estimate equivalent magnitudes of historical events from macroseismic intensities, information which is important for seismic hazard evaluation.

2. Several magnitude scales are generally used to characterize small events, some of them based on record duration, others on *S*-wave amplitudes or on coda characteristics. Historical or practical reasons have governed these practices; however, only a magnitude based on a seismic moment has a physical significance and must be obtained even for small events.
3. There is still a discussion on stress-drop scaling with magnitude (e.g., Mayeda and Walter, 1996; Ide and Beroza, 2001). The question is whether this parameter, which despite valid criticism is still called stress drop (Atkinson and Beresnev, 1997), should be considered as independent of magnitude.
4. Rock site conditions have to be characterized. Velocimetric stations set up for seismic surveys are usually located on hard rock. By contrast, most of the strong-motion stations are located in urban areas on weathered sedimentary soft rock sites. As shown by Steidl *et al.* (1996), Boore *et al.* (1997), and Lussou *et al.* (2001), differences in rock site conditions strongly affect the amplitude and the frequency content of strong motions. It is thus important to quantify site responses, including rock site responses, which are often used as reference sites for spectral ratio computations.

In this article, we wish to address these questions. A large number of studies about inversion of source, path, and site effects have been published (e.g., Andrews, 1986; Boatwright *et al.*, 1991; Ordaz and Singh, 1992; Field and Jacob, 1995; Raoof *et al.*, 1999; Bay *et al.*, 2003; Rietbrock *et al.*, unpublished manuscript). We use a method based on a two-stage analysis of the seismic spectra of the *S* wave, following Scherbaum and Wyss (1990) and Rietbrock (2001). The first stage consists in determining the geometrical spreading from a regression of the low-frequency flat level of the displacement spectra versus hypocentral distance. The second consists in a regression of the displacement corrected for the source term, versus frequency; this enables recovery of the corner frequency, the anelastic attenuation, and a frequency-dependent site effect. The method is applied to Pyrenean data. The Pyrenees are one of the most seismically active regions in France and Spain, with moderate magnitude events. No specific attenuation curve is available for this area, and almost nothing is known about stress drops of Pyrenean events. Site conditions are also not characterized for the Pyrenean stations.

We have focussed on *S* waves, which provide useful information for earthquake engineering purposes. Accelerometric and velocimetric stations have recorded a large number of events, providing high-quality data for such a study. For the smallest events, the velocimetric records make it possible to increase the distance range where no accelerograms are available. For such records, the amplitude of the low-frequency part of the spectra is attenuated by the instrument transfer function. Thus, the velocimetric data at frequencies significantly lower than the seismometer eigenfrequency (1 Hz) are not reliable, in spite of a rigorous deconvolution of the instrument response. Such a difficulty does not exist for the accelerometric records, which represent the largest data set at short distances.

The Pyrenean Context

The Pyrenean range has resulted from the collision of the Iberian and Eurasian plates with a low convergence rate. The suture between the two plates, the North Pyrenean fault (Fig. 1), is characterized by a sharp Moho jump. The crustal thickness increases from 30 km to the north of the range to 40–50 km to the south (Hirn *et al.*, 1980; Roure *et al.*, 1989). There is seismic activity along the whole range, with about 35 events of magnitude $m_b \geq 3.0$ each year (Souriau and Pauchet, 1998; Souriau *et al.*, 2001).

Since 1997 a seismic network of 20 three-component velocimetric stations has been operating in the French Pyrenees to survey the range. It is managed by the Observatoire Midi-Pyrénées (OMP). Twenty other stations are active on the Spanish side of the range. By combining the data from these networks, the OMP publishes yearly bulletins of the regional seismicity (www.omp.obs-mip.fr/omp/rssp/). In addition, the French Environment Ministry has decided to deploy a permanent accelerometric network in its territory. Nineteen stations were installed between 2001 and 2004 on the French side. The data are available at a central site located at the Grenoble Geophysical Observatory (www-rap.obs.ujf-grenoble.fr). The combined data from these two networks allows for good recording of earthquakes for a large range of distances and magnitudes.

Several magnitude scales are currently used. The OMP uses the classical M_L magnitude scale based on the maximum amplitude of the vertical record, with a decay curve valid for Californian data (e.g., Richter, 1958). At the national level, the Réseau National de Surveillance Sismique (RéNaSS) at Strasbourg uses a similar approach, with a specific amplitude decay of the form $a\Delta^b$ (Δ, epicentral distance and a, b, constants), compatible with Richter's M_L scale. The Laboratoire de Détection Géophysique (LDG) of the Atomic Energy Commission uses another French magnitude scale based on the amplitude of the L_g wave at distances of 100 to 500 km, with a distance correction defined for the whole national territory. These various procedures, which are derived from those developed for other countries, are not necessarily valid for the Pyrenees, and may result in biased magnitude estimations. A magnitude computation based on a

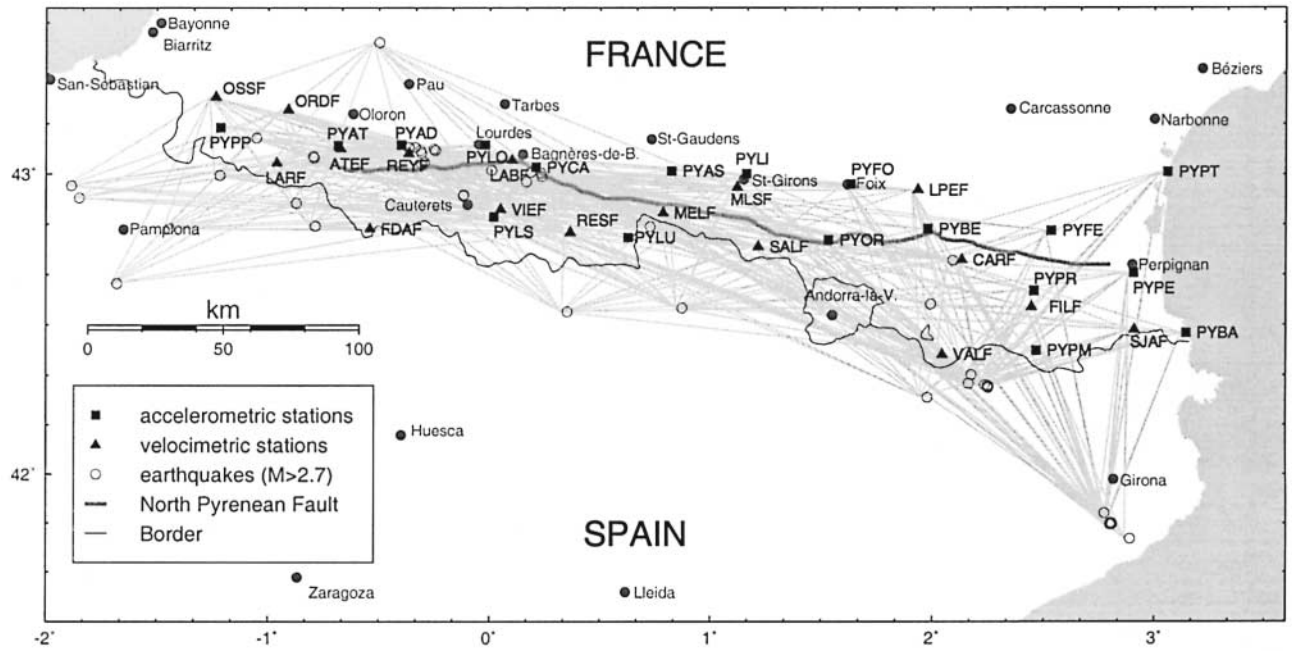

Figure 1. Map of the stations, events, and paths used in this study. Squares, accelerometers; triangles, velocimeters; open circles, epicenters. The North Pyrenean fault (hidden beneath the sediments to the west) corresponds to the boundary between Iberian and Eurasian plates and to a strong Moho jump (see text).

seismic moment with use of an appropriate amplitude decay is thus one of the goals of this study.

Numerous previous studies of crustal attenuation have been conducted in France, but most of them concern L_g-wave or *S*-wave coda (e.g., Campillo *et al.*, 1985; Campillo and Plantet, 1991; Chevrot and Cansi, 1996; Lacombe *et al.*, 2003). Only a few studies specifically concern the Pyrenees. Modiano and Hatzfeld (1982) used *S*-wave displacement spectra of local events in the western Pyrenees to estimate a frequency-independent quality factor, as well as seismic moments and stress drops. They found Q in the range of 200 to 300. In the same region, a study of coda Q (Herráiz and Mezcua, 1984) led to a mean Q-value of 400, which again is assumed to be independent of frequency. These authors also proposed an empirical relationship between the seismic moment M_0 and the local magnitude M_L. Again in the same area, Gagnepain-Beyneix (1987) analyzed coda waves and showed that scattering is the prevailing mechanism of attenuation below 10 Hz. She modeled the quality factor as $Q(f) = q_0 f^{\alpha}$ and observed strong variations of q_0 and α, both laterally and with depth. q_0 ranges from 30 to 140 and α from 0.7 to 1.1, low q_0 and high α being related to fractured areas in the upper crust. A very low coda-Q has also been observed in the eastern Pyrenees (Correig *et al.*, 1990). L_g waves for transpyrenean paths (Chazalon *et al.*, 1993) have been used to simultaneously invert Q and source parameters, assuming that the geometrical attenuation is known. A systematic underestimation of the moment magnitude M_w was observed, when compared to M_L. Up to now, no study is available at the scale of the whole Pyrenean range with a single method. Moreover, simultaneous inversion of geometrical attenuation, anelastic attenuation, source parameters, and site effects has not been attempted yet.

Data Selection and Spectrum Computation

Data from 18 accelerometric stations and 17 velocimetric stations have been used (see Table 1). All of these stations are located on the French side of the range, which is also the most active one. Unfortunately, no Spanish accelerometric data were available at the time of this study. The station characteristics are given in Table 1 as well as the nature of the ground where they are set up. The sampling rate is 125 samples per second for the accelerometers and 62.5 samples per second for the velocimeters.

In the initial selection, events with fewer than three accelerometric records were removed. Owing to the progressive deployment of the accelerometric stations from 2001 to 2002, only 45 events had three or more records (see Table 2). These have local OMP-magnitudes ranging from 2.7 to 5.4. For each event, stations at epicentral distances between 15 and 200 km have been selected. As will be seen in the Method section, the far-field approximation procedure requires a minimum distance of about 15 km. The cutoff at large distance was determined by our choice to work with S_g waves, and to avoid S_n and L_g waves, which could possibly lead to different results.

Figure 1 shows the paths between earthquakes and stations investigated in this study. Figure 2 gives the distribution of the data as a function of epicentral distances and

Table 1
Stations Used in This Study

Name	Lat. (deg. N)	Long. (deg. E)	Elevation (m)	Geological Site Type
Accelerometric Stations				
PYAD	43.098	−0.426	450	rock
PYAS	43.012	0.797	430	sediment
PYAT	43.095	−0.711	340	rock
PYBA	42.474	3.117	70	rock
PYBE	42.820	1.952	1080	rock
PYCA	43.024	0.183	701	rock
PYFE	42.814	2.507	275	sediment
PYFO	42.968	1.607	380	sediment
PYLI	43.002	1.136	424	rock
PYLO	43.098	−0.048	410	rock
PYLS	42.860	−0.008	770	rock
PYLU	42.791	0.601	630	sediment
PYOR	42.783	1.507	1030	rock
PYPE	42.673	2.878	100	sediment
PYPM	42.416	2.439	920	rock
PYPP	43.156	−1.241	270	rock
PYPR	42.614	2.429	410	sediment
PYPT	43.009	3.033	60	rock
Velocimetric Stations				
ATEF	43.086	−0.700	480	rock
CARF	42.716	2.106	1220	rock
FDAF	42.819	−0.567	1230	rock
FILF	42.560	2.418	850	rock
LABF	43.048	0.074	750	rock
LARF	43.038	−0.988	670	rock
LPEF	42.949	1.908	440	rock
MELF	42.873	0.759	940	rock
MLSF	42.958	1.095	450	rock
ORDF	43.214	−0.936	270	rock
OSSF	43.256	−1.262	240	rock
RESF	42.808	0.339	1270	rock
REYF	43.070	−0.393	480	rock
SALF	42.760	1.189	900	rock
SJAF	42.485	2.882	450	rock
VALF	42.402	2.017	1580	rock
VIEF	42.884	0.024	1000	rock

magnitudes. It shows that velocimetric data allow the data set at large distances to be increased, in particular for small magnitudes.

The *S*-wave spectra are computed on windows that are 20 sec long, beginning 1 to 5 sec before the S_g arrival, depending on hypocentral distance. Such a short window prevents the perturbation of the S_g signal by the coda and L_g wave at large distance. The coda might influence our results if longer windows were used. At the largest distances, S_n may arrive before S_g. However, this signal is weak and difficult to identify due to the varying Moho depth across the North Pyrenean fault; thus S_g, which is more energetic, will be used at any distance for spectrum computations.

For each record, the Fourier spectrum of the signal is computed after removing the linear trend, and is then corrected for instrumental response in the spectral domain using the transfer functions of the sensors (velocimeters Mark Products L4C [1 Hz]; accelerometers, Kinemetrics episensor), and the amplifications of the recorders. It is then divided by ω (where $\omega = 2\pi f$, with f the frequency) for the velocimetric data and by ω^2 for the accelerometric data, in order to obtain the displacement spectrum. The spectrum is then smoothed between 0.5 and 30 Hz for accelerometric data, between 0.5 and 15 Hz for velocimetric data, with the upper limits reflecting the different sampling rates of the two kinds of records. The smoothing is performed, for each spectrum, by computing the mean value over frequency bands of 1 Hz overlapping each other by 0.5 Hz. At low frequency ($f < 1$ Hz), windows are reduced to 0.5 Hz with 0.25 Hz overlap. This smoothing is applied in order to eliminate the very high frequency noise without eliminating the high-frequency content due to the site effects, and without oversmoothing the low frequencies. The level of smoothing remains, however, somewhat arbitrary.

The north and east components are combined in the Fourier domain to obtain a single horizontal component, such that

$$S(H) = \sqrt{\frac{S(E)^2 + S(N)^2}{2}} \quad (1)$$

This method assumes that the east and north components have no phase coherency, a hypothesis we checked in our records.

The noise spectra are computed in the same way on the signal between the beginning of the record and the *P*-wave arrival time. A minimum signal-to-noise ratio (S/N) of 3 is imposed for any frequency used in the inversion. The instrument correction amplifies noise at low frequency both for velocity and acceleration records. However, as the signal and noise spectra are amplified in the same way, the constraint on the S/N ratio rejects the frequencies for which the seismic signal is low. The high quality of the velocimetric sites allows the recovery of some significant signal (S/N >3) for magnitude 2.7 events up to 200 km.

Figure 3 shows the two horizontal records of the acceleration for the 16 May 2002 earthquake (14h56m) at the PYFO station, the raw and smoothed Fourier displacement spectra obtained for the horizontal signal, as well as the noise spectra. As expected, our displacement spectra reveal a flat level for frequencies greater than approximately 0.3 to 0.5 Hz followed by a decay at high frequency. A strong increase is also observed at very low frequency, but this is related to the division by ω or ω^2 or to the instrumental noise. As a test of robustness of the processing, we checked that the spectra obtained for the PYAT accelerometric station and the nearby ATEF velocimetric station were similar for all the events recorded by both stations (even for a magnitude 3.3 event up to 100 km; see Fig. 3c). This confirms that the instrumental correction is valid and that accelerometric and velocimetric data can be merged. The final data set consists of 588 spectra (184 from accelerometric records

Table 2
Earthquakes Used in This Study

N	Y	M	D	h:m	Lat. (deg. N)	Long. (deg. E)	Depth (km)	Magnitudes			Number of Records	Epicentral Distance Range (km) min/max
								OMP	LDG	RéNaSS		
1	2001	6	2	23h02m	42.259	1.951	5.7	3.7	3.6	3.9	11	16.8/172.4
2	2001	6	4	19h17m	43.007	0.160	11.4	3.4	3.6	3.6	14	17.6/190.9
3	2001	9	5	4h25m	43.089	−0.393	10.1	2.8	3.0	—	9	25.0/96.8
4	2001	10	7	18h24m	43.013	−0.018	9.4	3.1	3.2	3.1	11	31.1/179.6
5	2001	12	12	12h10m	43.121	−1.079	8.4	3.1	3.3	3.5	12	15.5/189.0
6	2001	12	14	18h28m	42.828	−0.814	8.9	3.4	3.5	3.6	14	27.3/163.6
7	2002	2	21	10h21m	42.921	−1.876	5.8	4.6	4.4	4.2	8	73.4/180.9
8	2002	3	18	15h18m	42.962	−1.912	6.2	4.3	4.1	3.7	7	62.1/184.2
9	2002	4	23	18h12m	42.827	0.701	5.9	2.8	2.9	3.0	9	29.6/139.8
10	2002	5	16	14h56m	42.929	−0.146	9.5	4.6	4.8	4.8	16	20.4/185.1
11	2002	5	16	15h14m	42.932	−0.144	7.1	4.3	4.4	4.2	14	20.0/185.0
12	2002	5	19	4h44m	42.975	0.140	12.5	3.7	3.8	3.8	20	17.6/197.9
13	2002	6	11	18h56m	41.832	2.783	9.3	3.2	3.0	3.0	10	70.9/186.8
14	2002	6	13	10h42m	41.835	2.780	8.6	3.3	3.2	3.4	12	70.5/186.4
15	2002	6	21	2h26m	41.830	2.772	8.9	4.0	3.7	3.6	11	70.7/187.1
16	2002	7	8	9h46m	43.033	−0.334	8.6	3.2	3.3	2.8	13	24.3/182.6
17	2002	7	16	9h26m	43.060	−0.822	8.4	3.0	3.0	3.2	8	19.4/167.2
18	2002	7	16	9h27m	43.055	−0.820	9.2	3.3	3.2	3.3	3	20.0/166.9
19	2002	9	5	20h42m	43.089	−0.390	9.3	4.0	4.1	4.1	10	25.2/187.4
20	2002	11	10	3h27m	42.638	−1.706	9.7	4.0	3.9	3.9	7	73.6/168.1
21	2002	11	28	18h30m	41.782	2.864	8.9	3.2	2.9	2.9	6	78.1/175.5
22	2002	12	9	13h44m	43.004	0.206	11.6	3.2	3.7	3.3	14	20.0/188.6
23	2002	12	11	20h09m	43.090	−0.364	11.8	4.2	4.3	4.4	13	25.7/185.3
24	2002	12	12	17h59m	43.080	−0.272	8.8	4.6	4.9	4.6	15	18.3/197.8
25	2002	12	13	6h00m	43.085	−0.280	8.9	3.0	3.3	2.9	13	18.9/198.6
26	2002	12	16	16h20m	42.545	0.325	8.8	3.3	3.3	3.3	18	29.2/172.4
27	2002	12	18	17h58m	42.993	0.210	13.0	2.8	3.2	2.4	13	19.4/161.7
28	2003	1	1	11h01m	42.904	−0.899	5.6	2.9	2.9	2.9	10	16.5/171.0
29	2003	1	21	18h01m	43.071	−0.335	9.1	4.3	4.6	4.4	14	23.5/182.9
30	2003	2	10	6h07m	43.079	−0.340	8.6	2.9	3.1	2.5	9	29.3/129.5
31	2003	2	26	3h32m	42.301	2.208	8.1	4.4	4.4	4.1	20	19.3/191.9
32	2003	3	10	0h54m	42.300	2.220	7.3	3.0	3.1	3.0	13	20.2/164.2
33	2003	4	18	2h54m	41.869	2.748	8.6	3.5	3.2	3.6	9	81.5/197.9
34	2003	7	2	6h45m	42.570	1.965	4.2	3.1	3.3	3.3	14	19.2/163.2
35	2003	9	30	5h31m	42.996	−1.243	7.9	3.3	3.4	3.4	12	21.3/199.9
36	2003	10	3	23h40m	42.714	2.064	11.1	3.3	3.5	3.5	18	29.1/167.5
37	2003	10	13	3h28m	43.436	−0.526	12.1	3.7	4.0	3.9	12	41.3/158.2
38	2003	10	26	8h28m	41.836	2.774	7.3	3.3	3.0	3.3	8	70.2/185.9
39	2004	2	3	21h16m	42.557	0.845	11.2	3.7	3.7	3.7	24	35.8/188.4
40	2004	6	1	16h50m	42.292	2.223	7.2	4.1	4.4	4.1	15	20.9/194.8
41	2004	6	4	4h56m	42.296	2.225	7.4	3.6	3.5	3.6	13	20.8/191.7
42	2004	6	4	18h24m	43.040	−0.322	6.5	3.2	3.4	3.2	13	31.1/181.6
43	2004	9	18	12h52m	42.819	−1.470	11.6	5.4	5.2	5.3	13	46.2/185.8
44	2004	9	21	15h48m	42.335	2.148	3.7	4.9	5.1	4.8	19	33.4/187.1
45	2004	9	23	9h58m	42.306	2.136	4.3	3.9	4.0	3.9	16	36.5/187.7

and 404 from velocimetric records) for 45 earthquakes and 35 stations.

A Qualitative Examination of the Acceleration Spectra

Before analyzing the displacement spectra, we shall first discuss the information in the accelerometric spectra. Figure 4 shows the spectra of the horizontal acceleration obtained at two stations (PYAT and PYAD) for different events. The distances are small, in the 30–60 km range, so the records are not strongly affected by anelastic attenuation. The spectra at PYAT (Fig. 4a) are typical of what is observed at most stations. At low frequency, we note an increase of acceleration with frequency, with a slope close to 2. This is characteristic of a Brune-type source (Brune, 1970, 1971). When the frequency increases, the spectra become asymptotically flat above the corner frequency f_c. This frequency, which is characteristic of the event, decreases for increasing magnitude. In the absence of attenuation, the spectra would remain

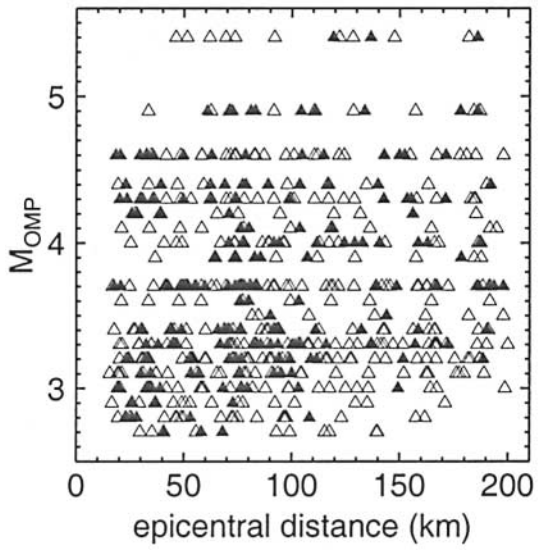

Figure 2. Magnitude versus distance for the events used in this study. Each symbol corresponds to one record, black triangles refer to accelerometers, and open triangles to velocimeters.

nearly flat up to the Nyquist frequency. However, a sharp fall-off is observed above $f_{max} = 20$ Hz. This f_{max}-value remains identical whatever the event and is characteristic of the station site (Hanks, 1982); even so, source effects have sometimes been invoked to explain it (Aki, 1987). For most of our stations, f_{max} is above 15 Hz, and the flat part of the spectra is only weakly perturbed by the site effects at lower frequency. For this reason, the frequency band 0.5–15 Hz will be used in the inversion.

Figure 4b gives an example where this is not the case. At the PYAD station, a sharp fall-off above 22 Hz is observed, but the spectra are not flat below that frequency, and it is hardly possible to identify the corner frequency from a change of slope. The site effect remains important around 5–10 Hz, and considerably distorts the spectrum shape. As most of the earthquakes are well recorded by a large number of stations (13 records for each event on average), we may expect that spectrum distorsions at a few stations will compensate for each other without introducing important biases in the final results.

Figure 5 shows the acceleration spectra of event 10 recorded at three stations with very different hypocentral distances. Taking into account the scaling factors on the right, a global attenuation by about 100 may be seen between the nearest and the most remote stations (29 km and 171 km). As will be seen in the next section, it is dominated at low frequency by the geometric attenuation. At large distances, the flat section between f_c and f_{max} does not become asymptotically horizontal as it did at a short distance. Rather, there is a decrease in amplitude with increasing frequency, which can be ascribed to anelastic attenuation. It is impossible to estimate either f_c or f_{max} visually for such large-distance spectra.

Method of Displacement Spectrum Analysis

The *S*-wave displacement spectrum $A_{ij}(r_{ij}, f)$ can be written as the product of a source term, a propagation term, and a station term:

$$A_{ij}(r_{ij}, f) = \Omega_i(f) \times D_{ij}(r_{ij}, f) \times S_j(f) \qquad (2)$$

where r_{ij} is the hypocentral distance from earthquake i to station j, and f is the frequency. The far-field displacement spectra of a Brune's source model (Brune, 1970, 1971) have been considered. As a minimum distance of a few wavelengths is required for the far-field approximation to be valid

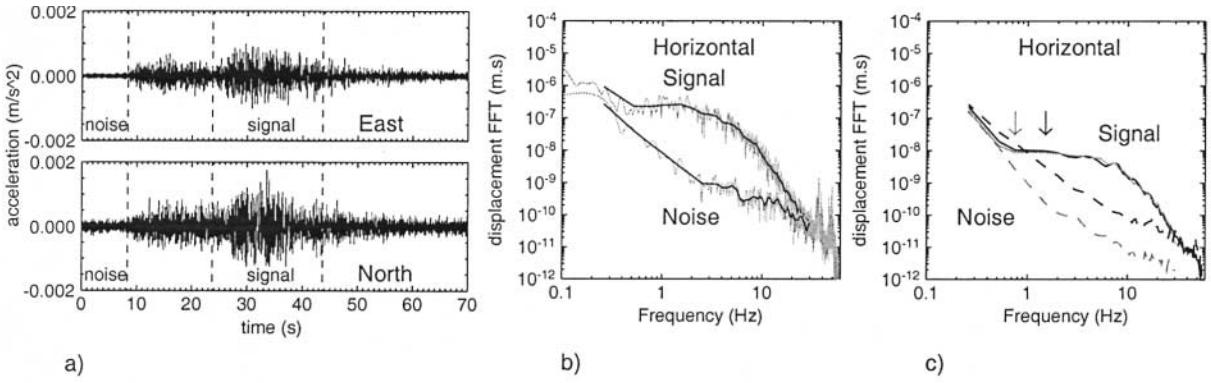

Figure 3. (a) Records of the acceleration for the horizontal components of the 16 May 2002 earthquake (14h56m) at the PYFO station. Vertical dashed lines delineate the windows used for spectrum computation of signal (between $t_S - 2$ sec and $t_S + 18$ sec) and noise. (b) Raw and smoothed Fourier spectra of the displacement (upper curve) and noise (lower curve) for this event. (c) Smoothed Fourier spectra (solid lines, signal; dashed lines, noise) of the 16 December 2002 earthquake ($M_{OMP} = 3.3$) recorded at PYAT (black) and ATEF (gray) (distance ~100 km). Arrows correspond to S/N = 3; lower frequencies are not taken into account in the inversion.

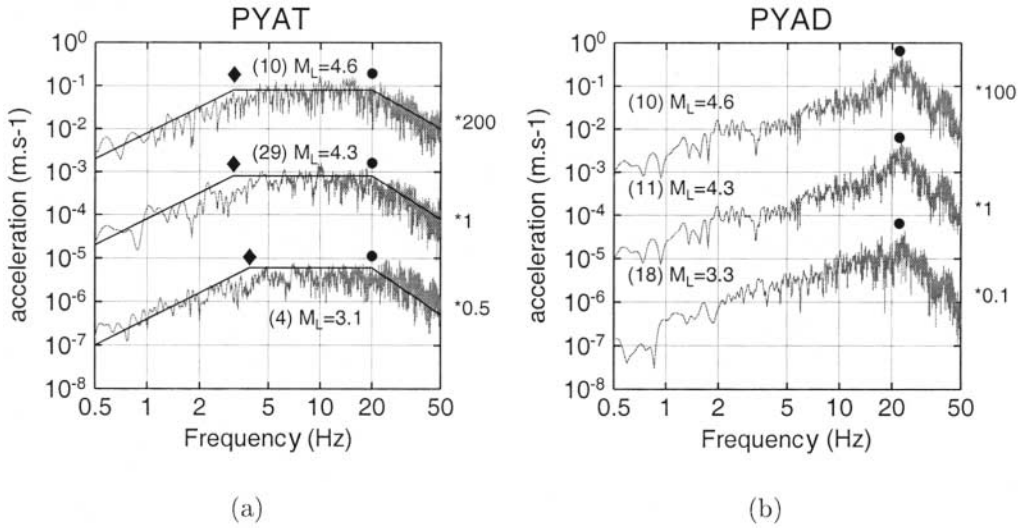

Figure 4. Examples of acceleration spectra for three events with different magnitudes recorded at two stations: (a) PYAT, which corresponds to typical spectra; (b) PYAD, where the spectra are very strongly distorted by an important site effect. The event number (in brackets) refers to Table 2. The multiplicative factor at the right of each spectrum were applied to the spectra so that they could be compared. Note, in (a) the apparent corner frequencies (diamond), and the fall-off above f_{max} (dot), a characteristic frequency of the station. In (b), the corner frequency for each event must be similar as in (a), but it is hidden by the site effect, and f_{max} is different with a stronger fall-off.

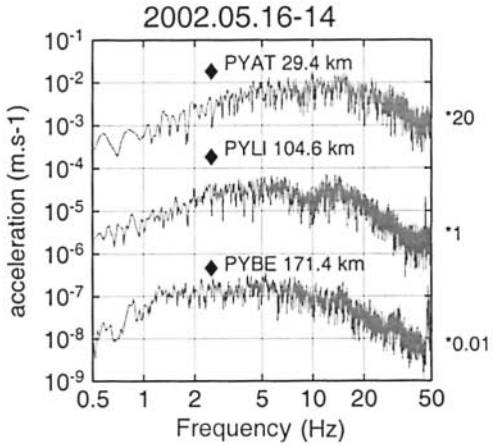

Figure 5. Acceleration spectra of event 10 at three stations with very different epicentral distances. Diamonds indicate the calculated corner frequency for this event (see Table 3). Note the change of the slope of the spectra between 3 and 20 Hz, mostly due to the anelastic attenuation.

(e.g., Aki and Richards, 2002), the use of frequencies down to 0.5 Hz (i.e., wavelengths up to 5 km) imposes a minimum hypocentral distance of about 15 km.

The attenuation along the path includes several mechanisms. First, the anelastic decay is represented by a term $\exp\left(-\frac{\pi r_{ij}}{Qv_S}f\right)$ where v_S is the average S-wave velocity along the path and Q the average quality factor, which is assumed to be frequency independent. The validity of this hypothesis will be discussed later. Second, we will assume that the geometrical spreading is allowed to differ from the classical $\frac{1}{r_{ij}}$ form, and can be written as $\frac{1}{R_0}\left(\frac{R_0}{r_{ij}}\right)^{\gamma}$, where R_0 is a saturation radius below which the decay in $r_{ij}^{-\gamma}$ is no longer valid. It is introduced to avoid a singularity at the origin. The scattering term is not introduced explicitly, so it may contribute to the geometrical spreading term if it is frequency independent, or it may appear as a perturbation in the anelastic term if it is frequency dependent.

$S_j(f)$ is the site effect at station j. This term is equal to unity at each frequency in the absence of a site effect.

Equation (2) may thus be written as:

$$A_{ij}(r_{ij}, f) = \frac{m_i}{1 + \frac{f^2}{f_{c_i}^2}} \times \exp\left(-\frac{\pi\, r_{ij}}{Qv_S} f\right) \times \frac{1}{R_0}\left(\frac{R_0}{r_{ij}}\right)^{\gamma} \times SF \times S_j(f) \quad (3)$$

This leads to a system of equations where the unknows are the m_i values (related to seismic moment) and the corner frequency f_{c_i} for each event i, the site term $S_j(f)$ for each station j, the parameters Q, γ, and R_0, which concern the propagation, and finally a frequency-independent scaling factor (SF), which is introduced at this stage to allow for fluctuations of the mean amplitude.

In order to simplify the resolution of system (3), we have adapted a method proposed by Scherbaum and Wyss

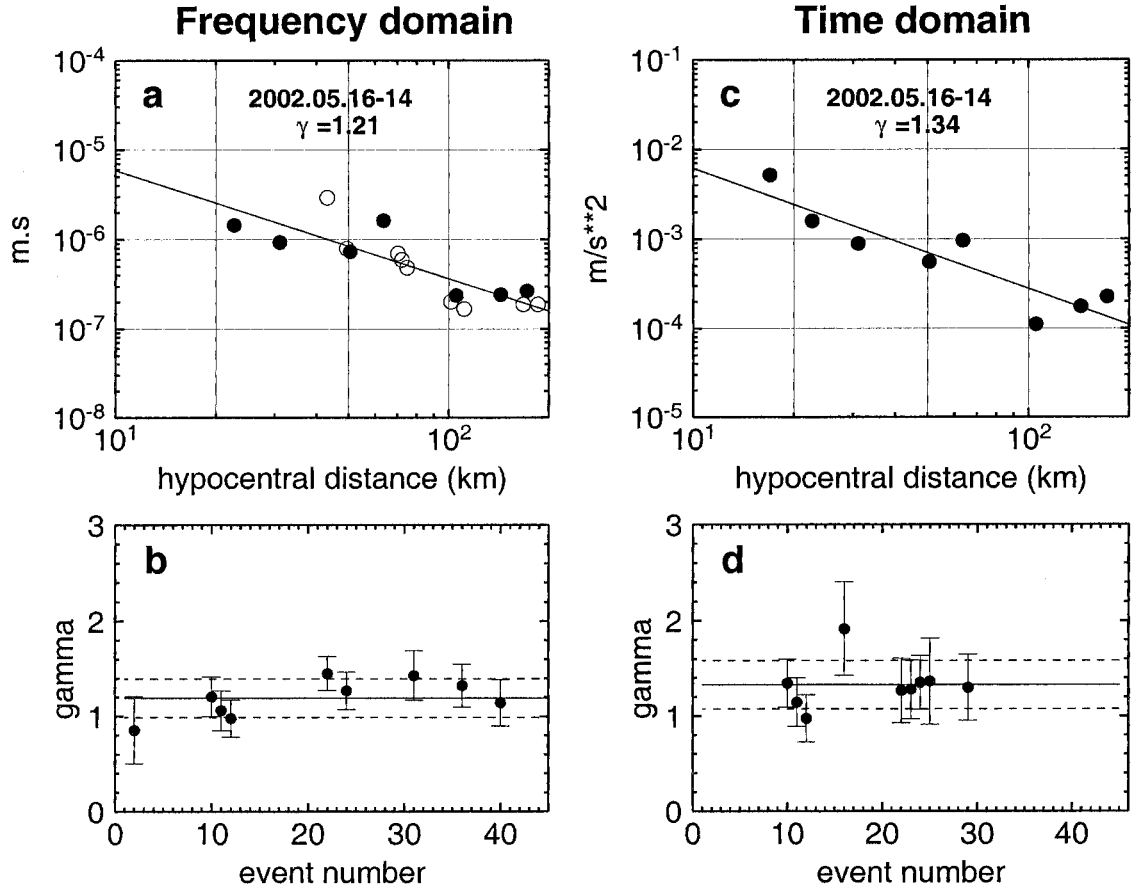

Figure 6. Determination of the geometrical spreading $1/r^{\gamma}$. (a) Example of event 10. Each dot gives the value of the low-frequency horizontal displacement spectrum at one station as a function of hypocentral distance. Dark symbols are for the accelerometric stations, open symbols for the velocimetric stations. The best fit (straight line) gives a slope $\gamma = 1.21$, and the distance between this line and the single values gives the station correction term, which is then averaged over all the records at the same station. (b) γ-values obtained for the best recorded events. Their mean value is $\gamma = 1.19$; dashed lines correspond to the 1σ confidence level. (c) and (d) Same as (a) and (b) determined in the time domain. (c) Peak ground acceleration of the east component records for event number 10, bandpass filtered at 0.5–2 Hz. (d) γ-values obtained for the best-recorded events.

(1990) and Rietbrock (2001). This consists in estimating separately the terms that determine the shape of the spectrum from those that depend on the distance and on the source.

Regression versus Distance at Zero Frequency: Retrieval of γ, SF, M_{0_i}, and R_0

The first step uses the expression of the displacement spectrum when the frequency becomes close to zero. By introducing the explicit expression of m_i (Brune, 1970), we get:

$$A(r_{ij}, f \rightarrow 0) = \frac{2R_{\theta\phi}M_{0_i}}{4\pi\rho\beta^3 R_0} \times SF \times \left(\frac{R_0}{r_{ij}}\right)^{\gamma} \qquad (4)$$

where $R_{\theta\phi}$ is the source radiation pattern, assumed to be constant ($R_{\theta\phi} = 0.63$ for S waves), M_{0_i} is the seismic moment, ρ and β are the density and the S-wave velocity of the medium at the source (we assume $\beta = v_S = 3.5$ km sec^{-1} and $\rho = 2800$ kg m^{-3}). The factor of 2 accounts for the free surface reflection at the station assuming a quasivertical incidence. This is exact for S_H and a convenient approximation for S_V (Modiano and Hatzfeld, 1982). Finally, R_0 is a reference distance below which the form of the attenuation is unknown. Taking the logarithm of equation (4), we find:

$$\log_{10}(A(r_{ij}, f \rightarrow 0)) = \log_{10}\left(\frac{2R_{\theta\phi}M_{0_i}}{4\pi\rho\beta^3 R_0}\right) + \log_{10}(SF) - \gamma \log_{10}\left(\frac{r_{ij}}{R_0}\right) \qquad (5)$$

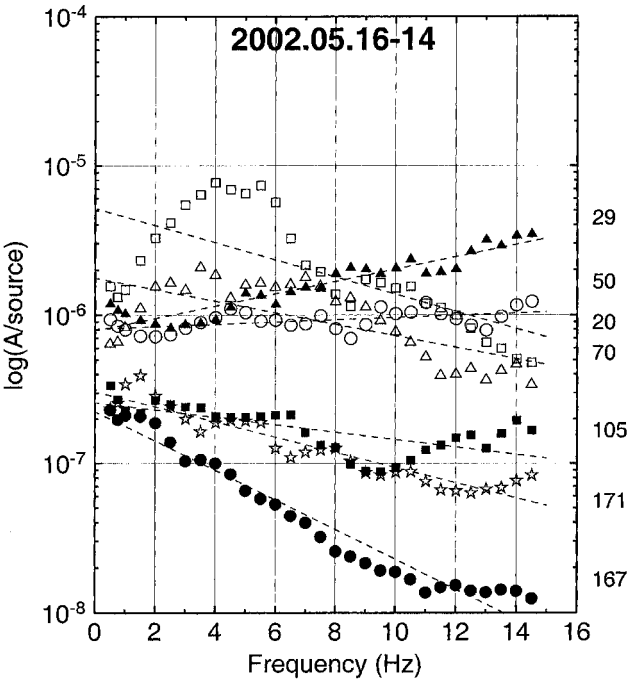

Figure 7. Determination of the anelastic attenuation from the Fourier displacement spectra (in ms), corrected for the source shape $\frac{1}{1+f^2/f_{c_i}^2}$. Example of event 10. The different symbols refer to the different stations with the epicentral distances shown (in km). Straight lines are obtained for the best-fitting corner frequency. The slopes are proportional to the ratio (distance/Q). Note the few unexpected negative slopes for short distances.

$A(r_{ij}, f \to 0)$ represents the flat part of the displacement spectrum at low frequency. We approximate it by calculating the mean value of $A(r_{ij}, f)$ in the frequency range 0.5–2 Hz, that is, below the corner frequency, which is of the order of 2.5 Hz for a magnitude 5 event (Chevrot and Cansi, 1996).

For a particular event, the exponent of the geometric attenuation is given by the slope of $\log_{10}(A(r_{ij}, f \to 0))$ as a function of $\log_{10}\left(\frac{r_{ij}}{R_0}\right)$. Figure 6a gives the example of event 10 (2002.05.16, 14h56m) recorded at 16 stations between 22.7 and 185.4 km, which gives a slope $\gamma = 1.21$. The γ-values are computed for the best-recorded events (Fig. 6b), and the mean value is taken as the geometrical spreading exponent for all the events.

Once γ is known, a correction for the geometrical spreading is applied to the $A(r_{ij}, f \to 0)$-values. For each event, a mean of these corrected values is computed, and the difference between the mean value (which depends on M_{0_i} and R_0) and the corrected value gives the frequency-independent scaling factor (SF) for the particular event considered at station j. Then, the average of these values for all the events recorded at station j gives a frequency-independent scaling factor per station.

Given γ and SF, M_{0_i} is obtained for each earthquake in the same way, by correcting the zero-frequency amplitude of each record for the geometrical spreading and for the scaling factor, and by computing the mean value. It should be noted that there is a trade-off between M_{0_i} and R_0, except for $\gamma = 1$ where R_0 vanishes. However R_0 remains independent of the event magnitude as long as the event is small, because an increase in M_{0_i} by a factor of k must result in an increase in $A(r_{ij}, f \to 0)$ by the same factor of k. R_0 corresponds to a volume in which the wave behavior in the vicinity of the source cannot be specified.

Regression versus Frequency: Retrieval of f_{c_i}, Q, and $S_j(f)$

In this section, we focus on the frequency-dependent terms. Equation (3) can be written as:

$$\log_{10}\left(\frac{A(r_{ij}, f)}{\frac{1}{1+\frac{f^2}{f_{c_i}^2}}}\right) = \log_{10}(A(r_{ij}\, f \to 0)) + \log_{10}(S_j(f)) - \frac{\pi r_{ij}}{2.3\ Q v_S} f \quad (6)$$

In the following sections, $\frac{A(r_{ij}, f)}{\frac{1}{1+f^2/f_{c_i}^2}}$ will be referred to as *A/source*.

In order to retrieve $1/Q$ and $S_j(f)$, a linear regression is applied to the system of equation (6). However, the linear dependence in frequency of system (6) is valid only for the exact value of the corner frequencies, so we first have to determine these values. For each event i, a full range of possible corner frequencies is tested by trial and error in the range 0.5–15 Hz, with steps of 0.1 Hz. The corner frequency is that which provides the best linear fit of the system of equation (6) simultaneously for all the records obtained at the different stations j. This is found by minimizing the residuals between $\log_{10}$ (*A/source*) and the linear fits of equation (6), but the frequency domain is limited to $f < 15$ Hz, in order to avoid the amplitude fall-off for $f > f_{max}$. A linear relationship is found between $\log_{10}(f_c)$ and M_{OMP}. It will be used to infer the corner frequencies used below, in order to avoid instabilities.

This is illustrated in Figure 7 for the 16 May 2002 (14h56m) earthquake (event 10 in Table 2), for a selection of stations where it was recorded. The different symbols refer to the different stations, and the dashed lines are the regressions versus frequency for the final value of corner frequency. Each slope gives the Q-value for the path linking the hypocenter to the station, and the fluctuations around the straight line are linked to the frequency-dependent term of the site effect $S_j(f)$.

Negative slopes are obtained for some stations, in particular at short distances, which are poorly affected by an-

elastic attenuation. This could be because of a trade-off between the corner frequency and the quality factor, as will be discussed later. This could also suggest that other mechanisms, such as scattering, have to be considered.

Results

Attenuation

Geometric Attenuation. As shown in Figure 6a, the γ-value obtained from the slope of $log_{10}(A_{ij}(r_{ij}, f \rightarrow 0))$ as a function of $\log_{10}(r_{ij})$, is correctly defined only if the hypocentral distances are widely distributed over a large range. We have thus selected events with at least 15 records, among which at least three are at a distance of less than 40 km. The slopes obtained (Fig. 6b) are consistent with each other, and lead to a mean geometric attenuation coefficient of $\gamma = 1.19 \pm 0.20$ (1σ error bar). Note that the use of the frequency range 0.5–2 Hz instead of the zero-frequency for defining $A(r_{ij}, f \rightarrow 0)$ may introduce a bias in the retrieved γ-value. For $Q = 360$, $r_{ij} = 100$ km and $R_0 = 1$ km, γ is overestimated by 0.1, according to (6). This value is of the same order as the error bar found for γ.

In order to test the γ-values, we performed a similar analysis in the time domain. Accelerometric data were bandpass filtered in the range 0.5–2 Hz, and for each event the peack ground acceleration of the filtered trace was plotted as a function of epicentral distance (Fig. 6c). Only accelerometric data were used in this test, thus fewer data are available, leading to larger error bars on the γ-values (Fig. 6d). The mean γ-value ($\gamma = 1.34 \pm 0.25$) is, however, very close to that of Figure 6a. It differs slightly from the usual value, $\gamma = 1$ obtained at teleseismic distances, but it is comparable to values reported in the literature for other regional studies (Malagnini and Herrmann, 2000; Bay *et al.*, 2003; Rietbrock *et al.*, unpublished manuscript). The value $\gamma = 1$, commonly used, is included in the 2σ confidence domain.

Anelastic Attenuation. This parameter is clearly the most poorly constrained in our study. Although the hypothesis of a frequency-independent Q is compatible with the linear trend in Figure 7, it would also be possible to fit the data with a parabolic trend, as would be expected if Q were of the form $Q(f) = q_0 f^{\alpha}$ Figure 8 gives the different $1/Q$-values obtained for each path with length greater than 50 km, as well as a histogram of these values. The shorter paths, which lead to very unstable results, have been withdrawn. For such paths, local heterogeneities have a large influence on the determination of Q, while for the long paths, an average of the Q factor is more likely to be obtained. Statistically, the most probable value of $1/Q$ is around 0.00075, leading to an unrealistic high quality factor of $Q \sim 1300$. This value is too high compared with those obtained by previous authors (Modiano and Hatzfeld, 1982; Gagnepain-Beyneix, 1987; Correig *et al.*, 1990; Chazalon *et al.*, 1993).

This result led us to suspect a trade-off between the quality factor and the corner frequency. We performed numerical tests to analyze the influence of a frequency-dependent quality factor on our linear inversion. We adopted a realistic quality factor of the form $Q(f) = 360 \times f^{0.3}$, which is rather far from the value we determined, but close to published values. Synthetic spectra were computed for the same paths as the real spectra, and the same parameters, but with this new Q-value and the corner frequencies derived previously. Our method assuming a frequency-independent Q was then applied to the synthetic data. As shown in Figure 9, it leads to erroneus corner frequencies, in particular for the smallest events, and to a $1/Q$-value of about 0.00075, corresponding to $Q \sim 1300$. It turns out that the actual quality

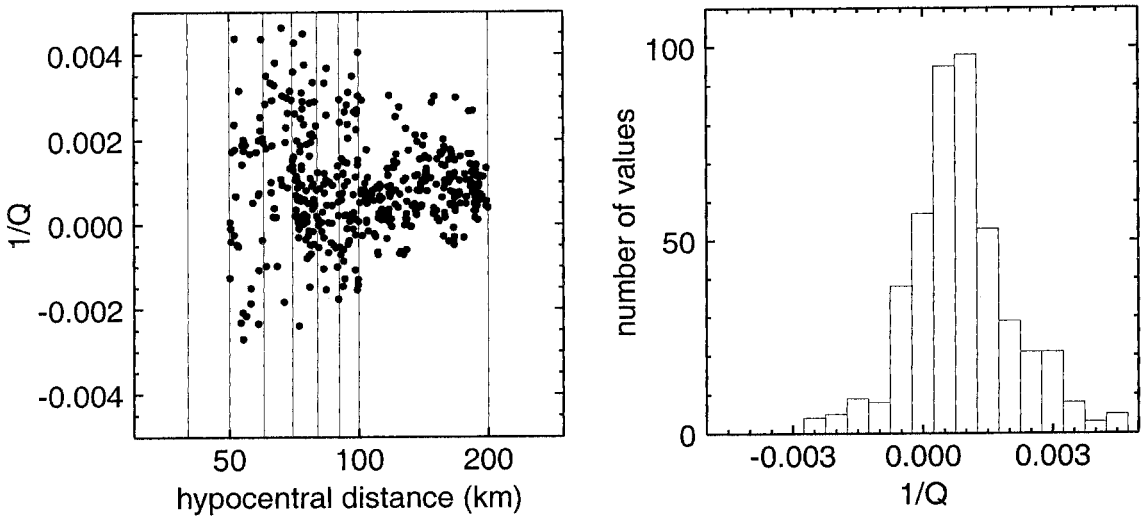

Figure 8. Anelastic attenuation $1/Q$-values determined for each record (left) and histogram of the results (right). Note the most probable value of attenuation $1/Q \sim 7.5 \times 10^{-4}$ leads to a very high Q-value ~ 1300.

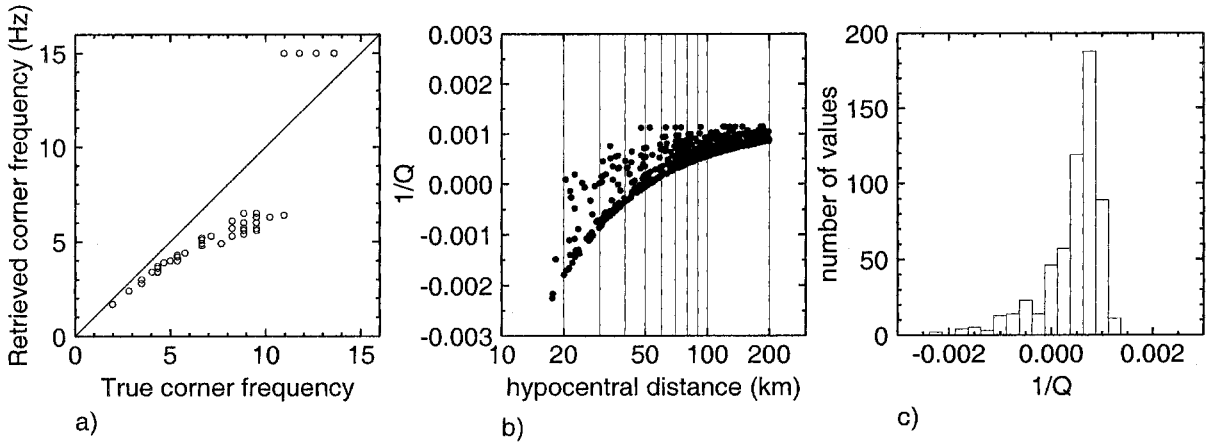

Figure 9. Numerical tests highlighting the trade-off between corner frequency and quality factor. The linear inversion has been applied to synthetic displacement spectra with $Q(f) = 360 \times f^{0.3}$, and for the same paths as in Figure 1. (a) Calculated corner frequencies versus input corner frequencies. (b) Attenuation values $1/Q$ versus hypocentral distance, and (c) histogram of these values.

factor in the Pyrenees is likely to be frequency dependent, and that a nonlinear inversion scheme is needed to resolve the Q-values. This will be developed more extensively in another article proposing a genetic inversion of the spectra.

Source Characteristics

Corner Frequency. Figure 10 shows the f_{c_i} domain scanned for performing the regression versus frequency, and the final corner frequencies obtained for each earthquake (dots) as a function of magnitude. Note that for some earthquakes the corner frequency is not retrieved, as the upper limit of the search domain is reached.

Taking into account the resolved corner frequencies, we derived a linear regression between $\log_{10}(f_{c_i})$ and the local magnitude M_{OMP} (solid line in Fig. 10): $\log_{10}(f_{c_i}) = 1.44\ (\pm 0.20) - 0.22\ (\pm 0.05)\ M_{\mathrm{OMP}}$. This may be compared to that obtained by Chevrot and Cansi (1996) for the French territory from L_g analysis. As they used the LDG magnitude scale, we rescaled their result to OMP magnitudes using the empirical relation: $M_{\mathrm{LDG}} = 0.89 \times M_{\mathrm{OMP}} + 0.5$ (Souriau and Pauchet, 1998). This gives: $\log_{10}(f_{c_i}) = 1.97 - 0.31 \times M_{\mathrm{OMP}}$ (see dotted line in Fig. 10). The agreement is good at large magnitude, for which both L_g and S give large amplitudes.

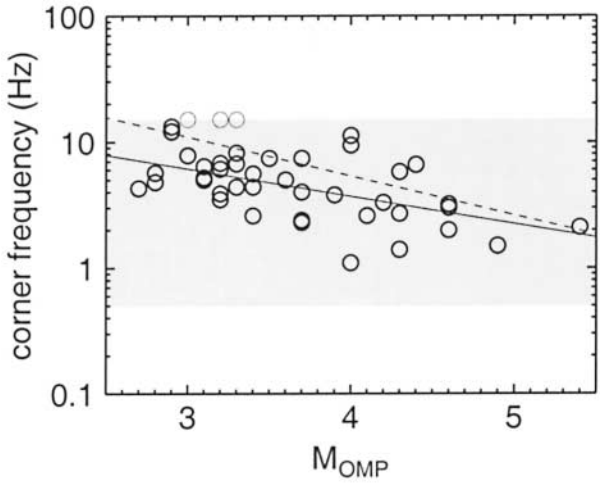

Figure 10. Corner frequency versus magnitude. The shaded area corresponds to the research domain; thick circles are the values obtained for each event from the inversion (thin circles are unresolved values), and the solid line is the best fit for the significant values. The dashed line corresponds to the values obtained by Chevrot and Cansi (1996) from L_g waves for France.

Seismic Moment and Stress Drop. The seismic moments cannot be determined independently from the reference distance R_0. A reference distance is always assumed by the authors, at least implicitly. For example, in most teleseismic studies the displacement is usually modeled as:

$$u(r,t) = \frac{1}{4\pi\rho v_S^3} R_{\theta\phi} \frac{1}{r} M_0 \qquad (7)$$

(e.g., Madariaga, 1976), which implicitly assumes that $R_0 =$ 1 km (in fact, $R_0 = 1$ in arbitrary units). If the radiation pattern is disregarded, it assumes that the energy is uniformly distributed on a sphere of radius unity around the focus. Another example at a regional scale is given by Richter (1958), who assumes that a magnitude zero earthquake corresponds to an amplitude of 10^{-3} mm at 100 km on a Wood–Anderson seismometer. Malagnini and Herrmann (2000), Malagnini, Herrman, and Di Bona (2000), and Malagnini, Herrmann, and Kosh (2000) consider a reference radius for both geometric and anelastic attenuation ranging

Table 3
Results (f_c and $\delta\sigma$ are Poorly Reliable for $M_{OMP} < 3.5$)

	M_L			$\gamma = 1.19$ $R_0 = 1$/km		
N	OMP	LDG	f_c (Hz)	M_0 (10^{12} N m)	M_w	$\Delta\sigma$(10^5 Pa)
1	3.7	3.6	4.0	12.6	2.67	1.88
2	3.4	3.6	2.6	11.6	2.64	0.46
3	2.8	3.0	4.8	3.2	2.27	0.66
4	3.1	3.2	5.2	3.1	2.26	0.82
5	3.1	3.3	5.0	4.7	2.38	1.11
6	3.4	3.5	4.4	12.2	2.66	1.95
7	4.6	4.4	2.0	244.9	3.53	3.95
8	4.3	4.1	1.4	136.7	3.36	0.61
9	2.8	2.9	4.3	16.1	2.74	2.57
10	4.6	4.8	3.2	146.6	3.38	8.80
11	4.3	4.4	5.8	61.6	3.13	19.53
12	3.7	3.8	2.4	22.1	2.83	0.61
13	3.2	3.0	3.9	5.1	2.40	0.56
14	3.3	3.2	5.6	3.9	2.33	1.24
15	4.0	3.7	11.2	15.8	2.73	107.62
16	3.2	3.3	6.1	4.6	2.37	2.08
17	3.0	3.0	7.8	3.2	2.27	2.96
18	3.3	3.2	6.7	5.1	2.40	2.95
19	4.0	4.1	9.4	21.8	2.83	36.51
20	4.0	3.9	1.1	69.3	3.16	0.19
21	3.2	2.9	6.8	15.1	2.72	9.16
22	3.2	3.7	3.5	6.8	2.49	0.70
23	4.2	4.3	3.3	51.0	3.07	3.06
24	4.6	4.9	3.0	177.9	3.43	10.68
25	3.0	3.3	—	18.1	2.77	—
26	3.3	3.3	—	6.0	2.45	—
27	2.8	3.2	5.7	1.9	2.13	0.69
28	2.9	2.9	13.2	2.5	2.20	9.10
29	4.3	4.6	2.7	71.4	3.17	2.53
30	2.9	3.1	12.1	10.7	2.62	40.19
31	4.4	4.4	6.6	66.2	3.15	34.97
32	3.0	3.1	—	8.2	2.54	—
33	3.5	3.2	7.4	5.9	2.45	4.84
34	3.1	3.3	6.4	3.4	2.28	2.03
35	3.3	3.4	8.2	6.3	2.47	0.60
36	3.3	3.5	—	3.8	2.32	—
37	3.7	4.0	2.3	32.3	2.94	0.69
38	3.3	3.0	4.4	7.8	2.53	1.44
39	3.7	3.7	7.4	11.3	2.64	8.15
40	4.1	4.4	2.6	30.2	2.92	0.95
41	3.6	3.5	5.0	9.6	2.59	2.14
42	3.2	3.4	—	3.3	2.28	—
43	5.4	5.2	2.1	1239.6	4.00	19.98
44	4.9	5.1	1.5	584.2	3.78	5.78
45	3.9	4.0	3.8	59.3	3.12	6.56

from 10 to 100 km. In the present study, we assume that this distance corresponds to a small sphere around the source, in which the energy is produced and outside of which the energy decays as $r^{-\gamma}$. Two distances were tested: 1 and 5 km (assuming $\gamma = 1.19$), and in each case the seismic moment was converted into moment magnitude using Kanamori's formula (Kanamori, 1977):

$$M_w = \frac{\log_{10}(M_0) - 9.1}{1.5} \quad (8)$$

with M_0 in N m (see Table 3). In order to determine the validity of the magnitude estimates, we compared them to the different local magnitudes used in France (Fig. 11). In each case, the moment magnitudes are 0.5 to 1 unit smaller than the local magnitudes, the difference increasing slightly with increasing R_0. The misfit between moment magnitudes and local magnitudes also increased with event magnitude. As a comparison, Figure 11c shows the same results with a standard geometric attenuation, $\gamma = 1$ and $R_0 = 1$ km, as in equation (7). The results are not significantly different. Assuming $\gamma = 1.2$ and $R_0 = 1$ km, we get the relation: $M_w = 0.64 \times M_L + 0.43$. This is very close to the result of Herráiz and Mezcua (1984) for a local study around the Pyrenean stations PYAT and ATEF, which leads to: $M_w = 0.69 \times M_L + 0.49$, once M_0 has been converted into M_w using (8). These results are consistent with the theoretical prediction $M_w \sim M_L/1.5$ obtained when the stress drop is assumed to be constant, as shown by Havskov (personal comm., 2005).

Figure 12 shows the relationship between the seismic moment and the corner frequency. According to Brune (1970), the seismic moment M_0 is related to the radius of the circular source (r_s) by:

$$M_0 = \frac{16}{7} \Delta\sigma \, r_s^3 \quad (9)$$

where $\Delta\sigma$ is the stress drop. On the other hand, the corner frequency for S waves is also related to r_s by:

$$f_c = \frac{0.37\beta}{r_s} \quad (10)$$

Combining equations (9) and (10) leads to:

$$M_0 = \frac{16}{7} \Delta\sigma \left(\frac{0.37\beta}{f_c}\right)^3 \quad (11)$$

thus:

$$\log_{10}(M_0) = \log_{10}(0.12\beta^3\Delta\sigma) - 3 \log_{10}(f_c) \quad (12)$$

We computed independent values of seismic moments and corner frequencies; consequently stress drops could be estimated from equation (12). As f_c cannot be determined for some events (see Table 3), stress drops were not computed for these events. Figure 12 shows that the stress drops are scattered, but not dependent on seismic moments. Most of the values are between 1 and 10 bars. They are of the same order as the mean stress drop of 35 bars obtained by Modiano and Hatzfeld (1982) in the western Pyrenees, and the values of 10–30 bars obtained by Gagnepain-Beyneix (1985) in the same region. From a general point of view, the values obtained for weak motions seem to be smaller than those for strong earthquakes. For example, Kanamori and

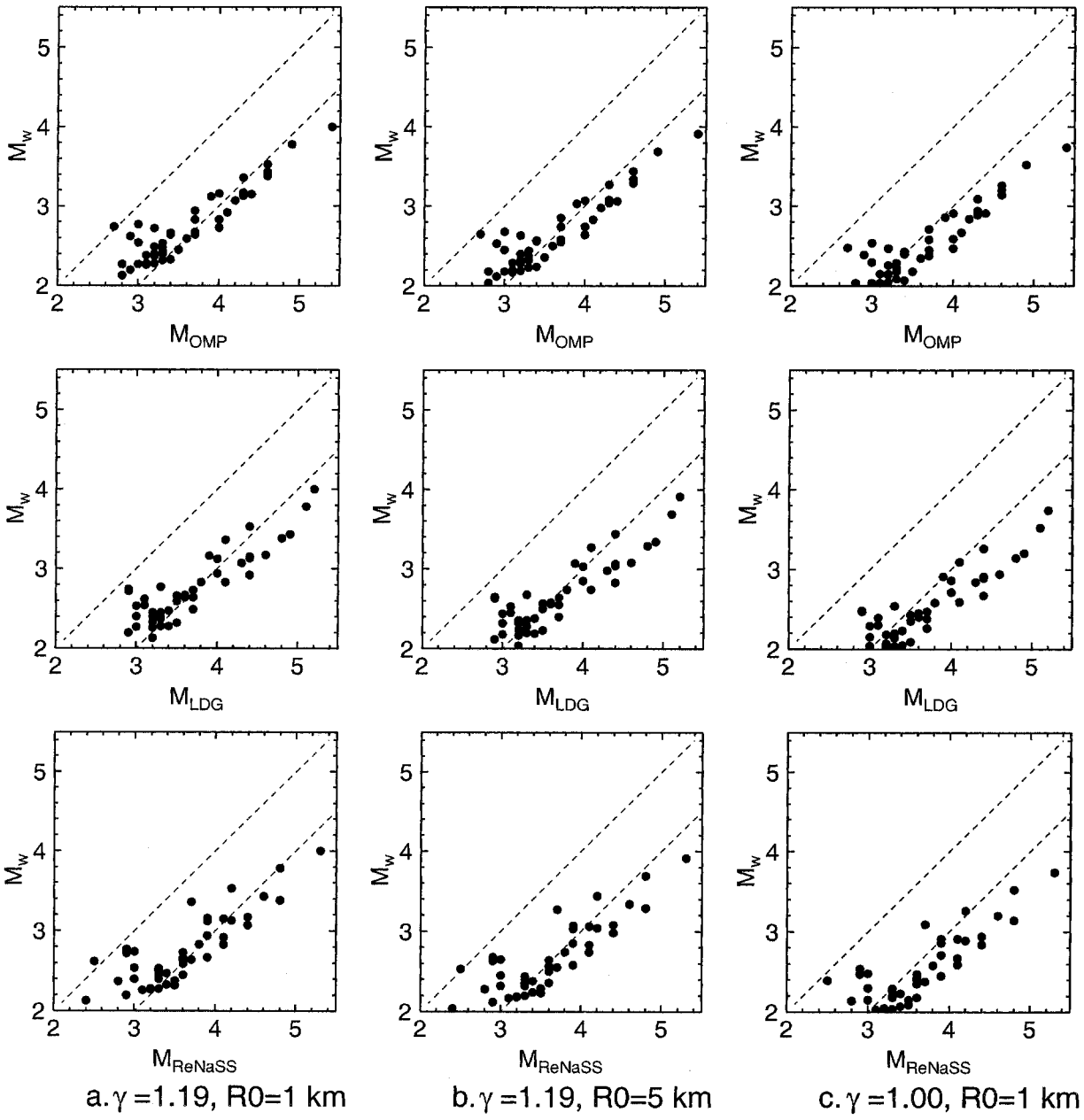

Figure 11. Moment magnitude as a function of the different magnitudes used in France (OMP, LDG, and RéNaSS) for $\gamma = 1.19$ and two values of the reference distance R_0 ([a] $R_0 = 1$ km and [b] $R_0 = 5$ km), and for $\gamma = 1$ ([c] $R_0 = 1$ km). Dashed lines indicate relations $M_w = M_L$ and $M_w = M_L - 1$.

Anderson (1975) found an average value of 100 bars for a worldwilde analysis of large intraplate earthquakes.

Site Effects

As it is obtained from the difference between the observed value of $\log_{10}(A/source)$ and the linear fit predicted by equation (6), the frequency-dependent site effect will depend on both the corner frequency and the Q-value. However, tests performed with different corner frequencies and different Q-values indicate that the frequency-dependent site effect remains stable, in spite of the trade-off outlined earlier. On the other hand, a constant term is retrieved at each station from the first step of the inversion (Fig. 13 and Table 4). However, its origin is not clear (see Field and Jacob, 1995), and it will not be discussed.

Figure 14 shows the frequency-dependent site effects derived from this study for the PYLO and PYPE stations for each earthquake (thin curves), and their mean value with one standard deviation (thick and dashed curves). Below 1 Hz,

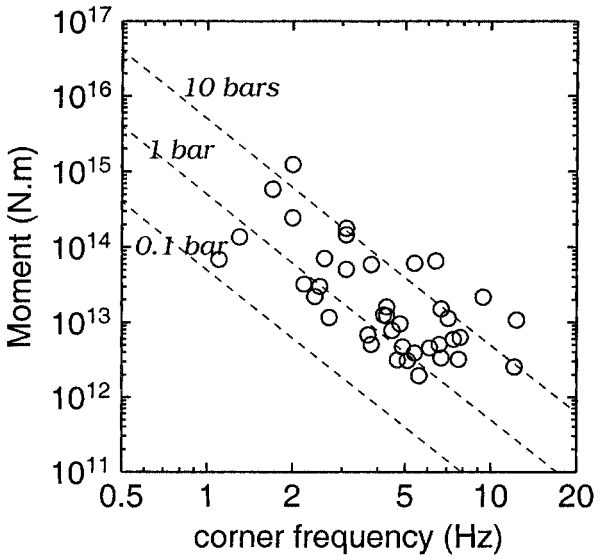

Figure 12. Seismic moment (computed with $\gamma = 1.19$ and $R_0 = 1$ km) versus corner frequency. The three dashed lines correspond to three different values of stress drop.

the results are somewhat unreliable, because the small events lack energy at low frequency. For the PYLO station there is a slight increase of the amplification from 1 to 5 Hz, followed by a strong fall-off between 5 and 7 Hz, and then a slow increase until 15 Hz. For station PYPE, there are two amplification peaks, at 2.5 and 5 Hz, and a strong increase near 15 Hz.

Following Field and Jacob (1995) and Chávez-García *et al.* (1999), it is interesting to compare site effects derived from the inversion with those from other methods. Site effects derived with the H/V noise method (Nakamura, 1989) have been calculated with the same set of data and for the same stations (see Fig. 15a and b). The general shape of the curves is in good agreement with those of Figure 14, but the amplitudes are considerably faded out. At the PYLO site, spectral ratios with reference station as well as H/V ratios were computed for a velocimetric station (CHA) located a few meters away from PYLO (Dubos *et al.*, 2003). The results are shown in Figures 15c and d. Both curves exhibit a peak between 2 and 5 Hz, as is also observed in our results. The differences in the high-frequency shape of the curves may be due to the methods used. In particular, results of Figure 15c may depend on the choice of the reference station.

Another interesting result concerns the site effects at stations located at rock sites. Figure 16 gives the reponses for these sites. Most of the stations have a nearly flat response, with a mean amplification of 1. However, we can identify two stations (PYLO and PYPM) that have a more complicated response. As shown by Steidl *et al.* (1996), near-surface weathering and cracking affect the recorded ground motion, and even stations located on rock sites may have a site effect.

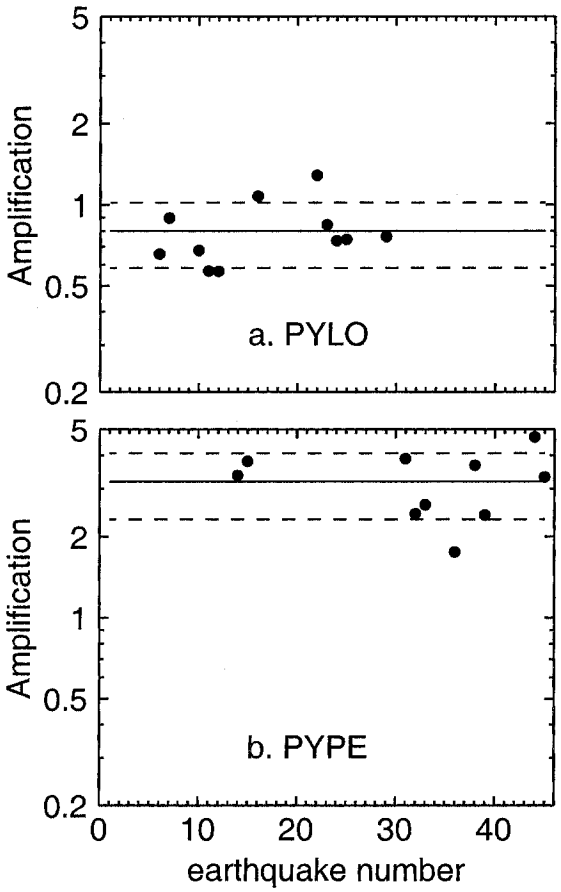

Figure 13. Scaling factor for the PYLO (a) and PYPE (b) stations, determined from the difference between the observed displacement at low frequency, and that predicted with a geometric attenuation as $1/r^{1.19}$. Note the amplification at PYPE ($\times 3.2$) and the amplitude decrease at PYLO ($\times 0.8$).

Table 4
Frequency-Independent Scaling Factors

Accelerometric Stations			Velocimetric Stations		
Name	Scaling Factor	1σ Error	Name	Scaling Factor	1σ Error
PYAD	0.82	0.26	ATEF	1.11	0.32
PYAS	0.65	0.11	CARF	0.76	0.30
PYAT	1.25	0.38	FDAF	1.68	—
PYBA	0.86	0.32	FILF	0.84	0.24
PYBE	1.11	0.34	LABF	1.46	0.87
PYCA	3.40	1.11	LARF	1.52	0.48
PYFE	1.14	0.29	LPEF	1.12	0.28
PYFO	1.06	0.19	MELF	0.82	0.21
PYLI	0.62	0.11	MLSF	0.65	0.26
PYLO	0.80	0.22	ORDF	1.19	0.37
PYLS	0.76	0.30	OSSF	0.96	0.39
PYLU	2.44	0.15	RESF	2.24	0.59
PYOR	0.68	0.17	REYF	0.90	0.37
PYPE	3.19	0.88	SALF	0.65	0.32
PYPM	1.66	1.25	SJAF	0.73	0.31
PYPP	1.68	0.68	VALF	2.25	2.57
PYPR	3.35	1.07	VIEF	0.95	0.50
PYPT	1.16	0.16			

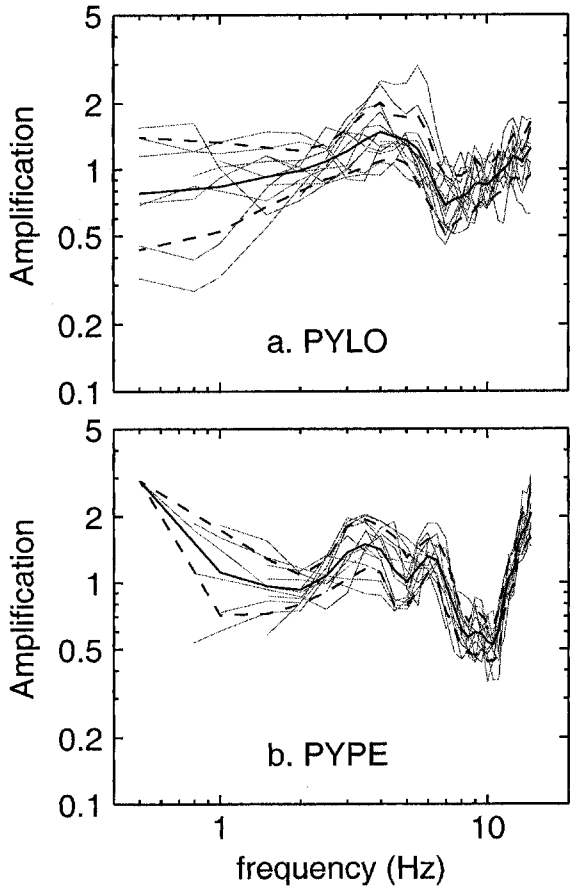

Figure 14. Frequency-dependent site effect obtained for the PYLO and PYPE stations in this study. Each thin line corresponds to one event; thick and dashed lines correspond to the mean ± one standard deviation.

Discussion and Conclusion

One of the goals of this study was to determine an empirical attenuation model for the Pyrenean range, and to define a simple procedure for computing moment magnitudes. We have shown that a two-step inversion based on very simple assumptions has allowed us to correctly determine the geometric attenuation, the source parameters (seismic moment and stress drop), and the site effects. The main hypotheses are a Brune-type source, a geometrical attenuation of the form $\frac{1}{R_0}\left(\frac{R_0}{r}\right)^{\gamma}$, and the validity of the far-field approximation, which prevents the use of data at distances less than about 15 km, for the frequency range (0.5–15 Hz) we investigated. We have also assumed that the *S*-wave velocity is the same beneath the source (β) and along the path (v_S). We have shown, in the various steps of our analysis, that these assumptions are justified. However, the difficulty to determine the low-frequency spectrum together with the trade-off between f_c and Q make it difficult to resolve these two parameters for the smallest events.

In order to see how well the model fits the data, we computed synthetic Fourier spectra with the parameters determined in this study (i.e., corner frequencies, Q, γ-value, seismic moments, reference distance, and site effects). Figure 17 shows the residuals between observed and computed spectra as a function of frequency and distance and a histogram of these residuals for earthquakes with magnitude greater than 3.5, for which the parameters (in particular the corner frequency) are assumed to be correctly determined. One can observe that over most of the frequency range (0.5–8 Hz), the difference between the logarithms of the spectra rarely exceeds 0.5. At a higher frequency, the influence of Q, f_c, and f_{max} leads to larger residuals.

The mean Q-value we obtained ($Q \sim 1300$) is not significant, as shown by the tests on synthetic data. Its determination could be considerably improved by assuming a frequency-dependent Q and performing a nonlinear inversion, as will be shown in another article. The shape of the spectra is also influenced by the site effects, in particular the f_{max} frequency. Its effect is, however, limited here by cutting the high-frequency part of the spectra at 15 Hz, but this also probably decreases the ability to resolve Q and the corner frequencies.

The frequency-independent attenuation (geometrical spreading) is represented by the $1/r^{\gamma}$ term, with a mean γ-value of 1.2. Numerous weak-motion studies report an attenuation slightly steeper than the classical $1/r$ variation (Malagnini and Herrmann, 2000; Bay *et al.*, 2003; Rietbrock *et al.*, unpublished manuscript). In all these studies, the exponent of the geometrical decay is distance dependent to account for the different types of waves present in the signal. In this work, no distance dependence is observed, but our distance range is limited to 15–200 km. Moreover, the window used to compute the spectra is such that it only includes S_g. We performed some tests using a window between the *S*-wave arrival time and two times the *S*-wave arrival time, which led to a geometric attenuation of the form $1/r^2$. This γ-value of 2 is close to that obtained from a coda analysis by Gagnepain-Beyneix (1987) in the western Pyrenees. Frankel *et al.* (1990) also found a geometrical decay as $1/r^2$ for *S* waves using the coda normalization method in southern California. This suggests that the coda influences the signal before twice the *S*-wave arrival time, which is often assumed to be the beginning of the coda. However Frankel *et al.* (1990) showed that, depending on the velocity structure, geometrical spreading can be steeper than r^{-1} at short distances (<100 km). They simulated this with a source located below a layered structure, and showed that some energy is reflected downward, leading to a supercritical geometrical attenuation. If such a mechanism is valid, then γ could be dependent on focal depth. We did not observe such a dependence with our data (i.e., see Fig. 6b and Table 2; earthquakes with different depths lead to similar γ-values).

Another important result concerns the source characteristics. The Brune-type source model assuming a single corner frequency and a f^2 fall-off seems realistic for the small

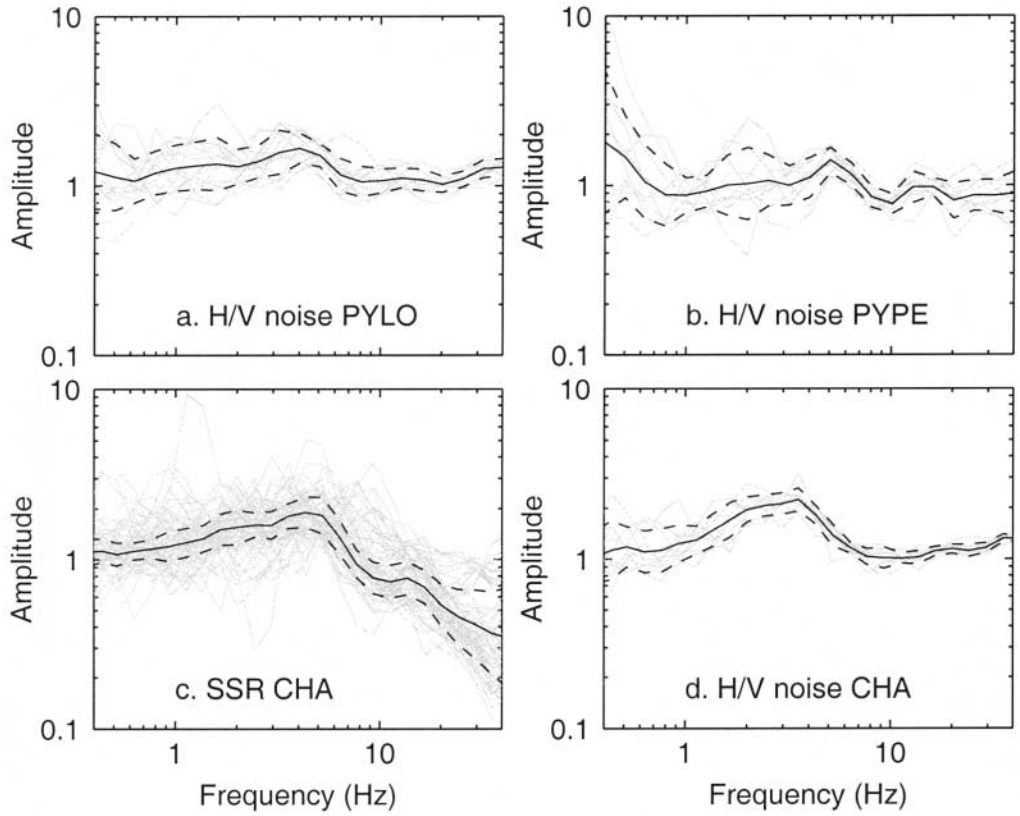

Figure 15. Site effects obtained for the PYLO and PYPE stations with other independent methods. (a) and (b), H/V noise with the same data set as in Figure 14; (c) and (d) spectral ratio with reference station and H/V noise for the CHA station located close to PYLO, from Dubos *et al.* (2003).

earthquakes analyzed here (see Fig. 7). The classical hypothesis of constant stress drop recently defended by Ide and Beroza (2001) seems to be valid for the Pyrenees in the magnitude range 2.7 to 5.4 (Fig. 12).

The magnitude computation from the flat part of the spectra leads to moment magnitudes that scale with the local magnitudes computed by the different institutions, as predicted by the theory, but they are systematically lower. The magnitude computation could certainly be improved by taking into account a 3D model for the crust, but such a model is not yet available with a sufficient definition for the whole Pyrenean range.

Finally, an interesting result of our study was the recovery of the site effects in a simple way, which gives an alternative to other methods, such as the H/V method and the spectral ratio with reference station method, based on different assumptions (no site effect on the vertical component for the former, and no site effect on the reference rock site for the latter). This study has also shown the advantage of deploying broadband velocimeters in seismic regions, as the recovery of the low-frequency part of the spectrum may be poor with short-period velocimeters and accelerometers. The low-frequency spectral component is crucial for a robust determination of both geometrical spreading and seismic moments.

Acknowledgments

We would like to thank D. Hatzfeld and P. Gueguen for managing the RAP, M. Sylvander for making the velocimetric data available to us, and J. F. Fels and S. Chevrot for helpful discussions on data processing and magnitude computation. We thank Associate Editor F. Chávez-García for his comments, which helped improve the manuscript. This work was supported by the CNRS with funding from the French Environment Ministry. The work of one of the coauthors (F.C.) has been funded by the Interreg IIIB Sismovalp project. We would also like to thank the reviewers, Jens Havskov and an anonymous reviewer, for their comments, as well as M. Bouchon for his help in finalizing the manuscript.

References

Aki, K. (1987). Magnitude-frequency relation for small earthquakes: a clue to the origin of f_{max} of large earthquakes, *J. Geophys. Res.* **92,** 1349–1355.

Aki, K., and P. G. Richards (2002). *Quantitative Seismology*, Second ed., University Science Books, Sausalito, California.

Ambraseys, N., K. A. Simpson, and J. J. Bommer (1996). Prediction of horizontal response spectra in Europe, *Earthquake Eng. Struct. Dyn.* **25,** 371–400.

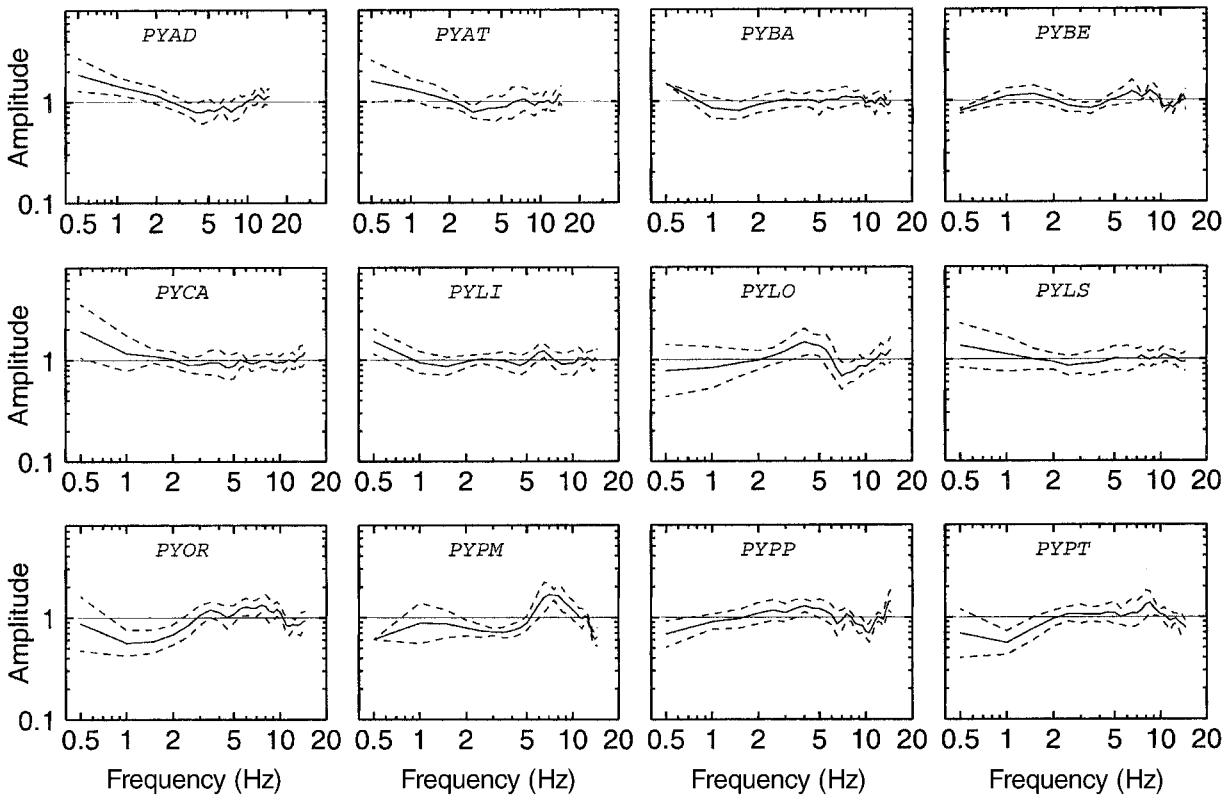

Figure 16. Site response for the stations classified as rock sites from their geological settings.

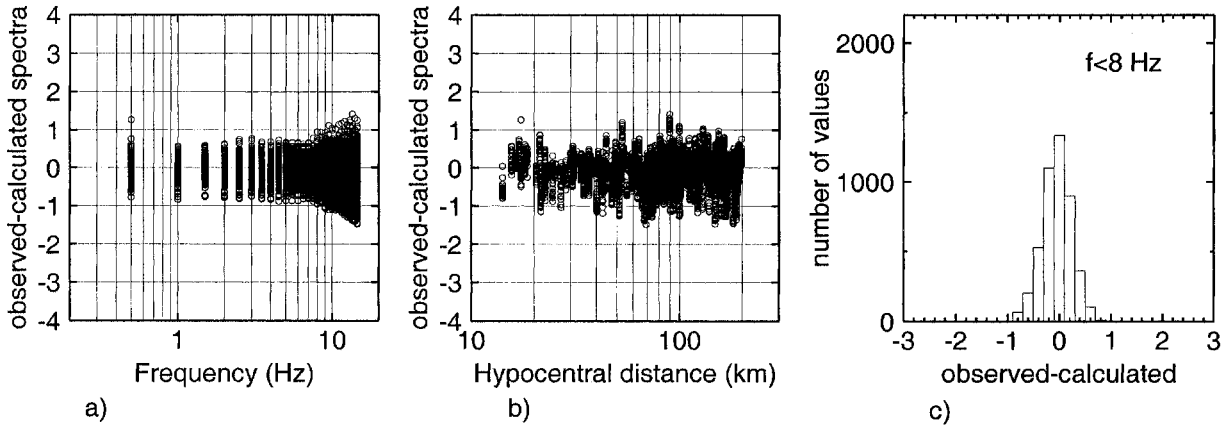

Figure 17. Differences between the decimal logarithms of the observed displacement spectra and those computed according to our model, for magnitudes $M_{OMP} < 3.5$. (c) Residuals distribution for frequencies less than 8 Hz.

Andrews, D. J. (1986). Objective determination of source parameters and similarity of earthquakes of different size, in *Earthquake Source Mechanics*, S. Das, J. Boatwright, and C. H. Scholz (Editors), American Geophysical Monograph 37, 259–267.

Atkinson, G. M., and I. A. Beresnev (1997). Don't call it stress drop, *Seism. Res. Lett.* **68,** 3–4.

Bay, F., D. Fäh, L. Malagnini, and D. Giardini (2003). Spectral shear-wave ground-motion scaling in Switzerland, *Bull. Seism. Soc. Am.* **93,** 414–429.

Berge-Thierry,C.,F.Cotton,O.Scotti,D.A.Griot-Pommera,andY.Fukushima- (2003). New empirical spectral attenuation laws for moderate European earthquakes, *J. Earthquake Eng.* **7,** 193–222.

Boatwright, J., J. B. Fletcher, and T. E. Fumal (1991). A general inversion scheme for source, site, and propagation characteristics using multiply recorded sets of moderate-sized earthquakes, *Bull. Seism. Soc. Am.* **81,** 1754–1782.

Boore, D. (1983). Stochastic simulation of high-frequency ground motions based on seismological models of the radiated spectra, *Bull. Seism. Soc. Am.* **73,** 1865–1894.

Boore, D. M., W. B. Joyner, and T. E. Fumal (1997). Equations for esti-

mating horizontal response spectra and peak acceleration from western North American earthquakes: a sumary of recent works, *Seism. Res. Lett.* **68,** 128–153.

Brune, J. N. (1970). Tectonic stress and the spectra of seismic shear waves from earthquakes, *J. Geophys. Res.* **75,** 4997–5009.

Brune, J. N. (1971). Correction, *J. Geophys. Res.* **76,** 5002.

Campillo, M., and J.-L. Plantet (1991). Frequency dependence and spatial distribution of seismic attenuation in France: experimental results and possible interpretations, *Phys. Earth Planet. Interiors* **67,** 48–64.

Campillo, M., J.-L. Plantet, and M. Bouchon (1985). Frequency-dependent attenuation in the crust beneath central France from *Lg* waves: data analysis and numerical modelling, *Bull. Seism. Soc. Am.* **75,** 1395–1411.

Chávez-García, F. J., W. R. Stephenson, and M. Rodríguez (1999). Lateral propagation effects observed at Parkway, New Zealand. A case history to compare 1D versus 2D site effects, *Bull. Seism. Soc. Am.* **89,** 718–732.

Chazalon, A., M. Campillo, R. Gibson, and E. Carreno (1993). Crustal wave propagation anomaly across the Pyrenean range. Comparison between observations and numerical simulations, *Geophys. J. Int.* **115,** 829–838.

Chevrot, S., and Y. Cansi (1996). Source spectra and site-response estimates using the coda of *Lg* waves in Western Europe, *Geophys. Res. Lett.* **23,** 1605–1608.

Correig, A. M., B. J. Mitchell, and R. Oritz (1990). Seismicity and coda *Q* values in the Eastern Pyrenees: first results from the La Cerdanya seismic network, *Pageoph* **132,** 311–329.

Dubos, N., A. Souriau, C. Ponsolles, J. F. Fels, and G. Sénéchal (2003). Etudes des effets de sites dans la ville de Lourdes (Pyrénées, France) par la méthode des rapports spectraux, *Bull. Soc. Géol. Fr.* **174,** 33–44.

Field, E. H., and K. H. Jacob (1995). A comparison and test of various site-response estimation techniques, including three that are not reference-site dependent, *Bull. Seism. Soc. Am.* **85,** 1127–1143.

Frankel, A. (1991). Mechanisms of seismic attenuation in the crust: scattering and anelasticity in New York State, South Africa, and southern California, *J. Geophys. Res.* **96,** 6269–6289.

Frankel, A., A. McGarr, J. Bicknell, J. Mori, L. Seeber, and E. Cranswick (1990). Attenuation of high-frequency shear waves in the crust: measurements from New York State, South Africa, and southern California, *J. Geophys. Res.* **95,** 17,441–17,457.

Gagnepain-Beyneix, J. (1985). Variation of source parameters of small western Pyrenean earthquakes and their relation to main shock occurrence, *Ann. Geophys.* **3,** 381–394.

Gagnepain-Beyneix, J. (1987). Evidence of spatial variations of attenuation in the western Pyrenean range, *Geophys. J. R. Astr. Soc.* **89,** 681–704.

Geli, L., P.-Y. Bard, and B. Jullien (1988). The effect of topography on earthquake ground motion: a review and new results, *Bull. Seism. Soc. Am.* **78,** 42–63.

Hanks, T. C. (1982). *fmax*, *Bull. Seism. Soc. Am.* **72,** 1867–1879.

Herráiz, M., and J. Mezcua (1984). Application of coda wave analysis to microearthquake analog data, *Ann. Geophys.* **2,** 545–552.

Hirn, A., M. Daignières, J. Gallart, and M. Vadell (1980). Explosion seismic sounding of throws and dips in the continental Moho, *Geophys. Res. Lett.* **7,** 263–266.

Ide, S., and G. C. Beroza (2001). Does apparent stress vary with earthquake size?, *Geophys. Res. Lett.* **28,** 3349–3352.

Kanamori, H. (1977). The energy release in great earthquakes, *J. Geophys. Res.* **82,** 2981–2987.

Kanamori, H., and D. Anderson (1975). Theoretical basis of some empirical relations in seismology, *Bull. Seism. Soc. Am.* **65,** 1073–1095.

Lacombe, C., M. Campillo, A. Paul, and L. Margerin (2003). Separation of intrisic absorption and scattering attenuation from L_g coda decay in central France using acoustic radiative transfer theory, *Geophys. J. Int.* **154,** 417–425.

Lussou, P., Y. Fukushima, P. Y. Bard, and F. Cotton (2001). Seismic design regulation codes: contribution of Knet data to site effect evaluation, *J. Earthquake Eng.* **5,** 13–33.

Madariaga, R. (1976). Dynamics of an expending circular fault, *Bull. Seism. Soc. Am.* **66,** 639–666.

Malagnini, L., and R. B. Herrmann (2000). Ground-motion scaling in the region of the 1997 Umbria-Marche earthquake (Italy), *Bull. Seism. Soc. Am.* **90,** 1041–1051.

Malagnini, L., R. B. Hermann, M. Di Bona, and K. Kosh (1999). Ground motion attenuation at regional distance in Italy and Germany, *Seism. Res. Lett.* **70,** 214–225.

Malagnini, L., R. B. Herrmann, and M. Di Bona (2000). Ground-motion scaling in the Apennines (Italy), *Bull. Seism. Soc. Am.* **90,** 1062–1081.

Malagnini, L., R. B. Herrmann, and K. Koch (2000). Regional ground-motion scaling in central Europe, *Bull. Seism. Soc. Am.* **90,** 1052–1061.

Mayeda, K., and W. R. Walter (1996). Moment, energy, stress drop, and source spectra of western United States earthquakes from regional coda envelopes, *J. Geophys. Res.* **101,** 11,195–11,208.

Modiano, T., and D. Hatzfeld (1982). Experimental study of the spectral content for shallow earthquakes, *Bull. Seism. Soc. Am.* **72,** 1739–1758.

Nakamura, Y. (1989). A method for dynamic characteristics estimations of subsurface using microtremors on the ground surface, *Q. Rep. RTRI Jpn.* **30,** 25–33.

Ordaz, M., and S. K. Singh (1992). Source spectra and spectral attenuation of seismic waves from Mexican earthquakes, and evidence of amplification in the hill zone of Mexico City, *Bull. Seism. Soc. Am.* **82,** 43–24.

Raoof, M., R. B. Herrmann, and L. Malagnini (1999). Attenuation and excitation of three-component ground motion in southern California, *Bull. Seism. Soc. Am.* **89,** 888–902.

Richter, C. F. (1958). *Elementary Seismology*, Freeman, San Fransisco.

Rietbrock, A. (2001). *P* wave attenuation structure in the fault area of the 1995 Kobe earthquake, *J. Geophys. Res.* **106,** 4141–4154.

Roure, F., P. Choukroune, X. Berastegui, J. A. Munoz, A. Villien, P. Matheron, M. Bareyt, M. Seguret, P. Camara, and J. Deramond (1989). ECORS deep seismic data and balanced cross sections: geometric constraints on the evolution of the Pyrenees, *Tectonics* **8,** 41–50.

Sabetta, F., and A. Pugliese (1996). Estimation of response spectra and simulation of nonstationary earthquake ground motions, *Bull. Seism. Soc. Am.* **86,** 337–352.

Scherbaum, F., and M. Wyss (1990). Distribution of attenuation in the Kaoiki, Hawaii, source volume estimated by inversion of *P* wave spectra, *J. Geophys. Res.* **95,** 12,439–12,448.

Souriau, A., and H. Pauchet (1998). A new synthesis of Pyrenean seismicity and its tectonic implications, *Tectonophysics* **290,** 221–244.

Souriau, A., M. Sylvander, A. Rigo, J. F. Fels, J. M. Douchain, and C. Ponsolles (2001). Sismotectonique des Pyrénées: principales contraintes sismologiques, *Bull. Soc. Géol. Fr.* **172,** 25–39.

Steidl, J. H., A. G. Tumarkin, and R. J. Archuleta (1996). What is a reference site? *Bull. Seism. Soc. Am.* **86,** 1733–1748.

Laboratoire de Dynamique Terrestre et Planétaire
Observatoire Midi-Pyrénées
14, Avenue Edouard Belin
31400 Toulouse, France
(S.D., A.S.)

Laboratoire de Géodynamique Interne et Tectonophysique
Observatoire de Grenoble
BP 53X
38041 Grenoble Cedex, France
(F.C.)

Manuscript received 8 June 2004.